

Electronic band structure of the layered compound Td-WTe₂

J. Augustin,^{1,*} V. Eyert,^{2,3} Th. Böker,¹ W. Frentrup,^{1,†} H. Dwelk,¹ C. Janowitz,¹ and R. Manzke¹

¹Humboldt-Universität zu Berlin, Institut für Physik, Invalidenstrasse 110, 10115 Berlin

²Hahn-Meitner-Institut, Glienicker Strasse 100, 14109 Berlin

³Universität Augsburg, Institut für Physik, Universitätsstrasse 1, 86135 Augsburg

(Received 19 July 1999; revised manuscript received 3 March 2000)

We have studied the electronic structure of the layered compound Td-WTe₂ experimentally using high-resolution angle-resolved photoelectron spectroscopy, and theoretically using density-functional based augmented spherical wave calculations. Comparison of the measured and calculated data shows in general good agreement. The theoretical results reveal the semimetallic as well as metallic character of Td-WTe₂; the semimetallic character is due to a 0.5 eV overlap of Te 5*p*- and W 5*d*-like bands along Γ -*Y*, while the metallic character is due to two classical metallic bands. The rather low conductivity of Td-WTe₂ is interpreted as resulting from a low density of states at the Fermi level.

I. INTRODUCTION

For more than two decades, layered transition metal dichalcogenides (TMDC) have served as a kind of prototype material for the analysis of the momentum-resolved electronic structure of solids. Because of their layered structure, the electronic properties are quasi-two-dimensional, making this class of materials interesting for many experimental and theoretical investigations.^{1,2} The two dimensionality leads to a small dependence of the electronic structure on the wave-vector component perpendicular to the layers, k_{\perp} , and makes the TMDC's ideal candidates for comparing experimental and theoretical electronic band dispersions.

Wilson and Yoffe³ were the first to propose a simple band model to account for the trigonal prismatic coordination around the metal atoms of the Group-VIB diselenides and disulphides. This coordination is stabilized by the crystal-field induced lowering of the metal $d_{3z^2-r^2}$ orbital relative to the remaining *d* states.⁴ The ditellurides differ: except for the low-temperature polymorph α -MoTe₂ they display a distorted octahedral coordination around the metal atoms, which are displaced from the centers of the octahedra due to strong metal-metal bonding.

Although the electronic structure of the Group-VIB TMDC's has been intensively studied, very little work has been done on the Group-VIB ditellurides: *Ab initio* linear combination of atomic orbitals (LCAO) calculations of the electronic structure of Td-WTe₂ have been performed by Dawson and Bullett,⁴ who interpret the semimetallic ground state of Td-WTe₂ as being due to its reduced Madelung energy as compared to hypothetical 2H-WTe₂. The electronic properties of Td-WTe₂ have been likewise studied by Brixner⁵ and Kabashima,⁶ who used a three-carrier semimetal band model to explain the electrical resistivity.

The present paper is intended to complement the aforementioned studies on Td-WTe₂ on both the experimental and theoretical side. It is meant to provide a reference for further experiments on the electronic structure of Td-WTe₂. Therefore, we are presenting a combined experimental and theoretical study of the electronic structure of Td-WTe₂ crystals. To achieve this end, both high-resolution angle-resolved

photoemission spectroscopy and augmented spherical wave (ASW) electronic structure calculations, as based on density-functional theory (DFT) and the local-density approximation (LDA), have been used. The obtained good agreement between experimental and calculated results lays the ground for a comprehensive comparison and discussion. Slight deviations are discussed and can be explained. Of particular interest are the bands near the Fermi energy. By analyzing these bands we attempt to determine whether Td-WTe₂ can be classified as a classic semimetal. To this end, transport measurements have also been carried out, which reveal semimetallic resistivity. However, deviations from the simple semimetallic band scheme place Td-WTe₂ on the border between metal and semimetal.

The paper is organized as follows: In Sec. II we discuss the basic structural and electronic properties of Td-WTe₂. Before describing the experimental details in Sec. IV, we discuss the calculational method. Theoretical band structure is discussed in Sec. III. The characterization of the crystals is given in Sec. V and the photoemission data as compared to the theoretical results are presented in Sec. VI. There we show the complete valence-band structure along with the detailed band dispersion parallel and perpendicular to the layers. This is complemented by a comprehensive discussion of the experimental and theoretical results and by a summary.

II. STRUCTURAL AND ELECTRONIC PROPERTIES

In 1966, Brown's investigations showed that Td-WTe₂ crystallizes in a layered structure similar to that of the 1T polytype.⁷ The structure can be described as layers of tungsten atoms that bind two sheets of tellurium atoms into infinite two-dimensional layers. The bonds between the Te-W-Te sandwich layers are weak because they result from Te-Te van der Waals interactions. For this reason the space between the sandwiches is often called the van der Waals gap. The Td structure is shown in Fig. 1.

As in the 1T polytype, the tungsten atoms are octahedrally coordinated by tellurium atoms. However, in contrast to the 1T structure, successive sandwich layers are rotated 180°. Furthermore, the characteristic WTe₆ octahedra undergo

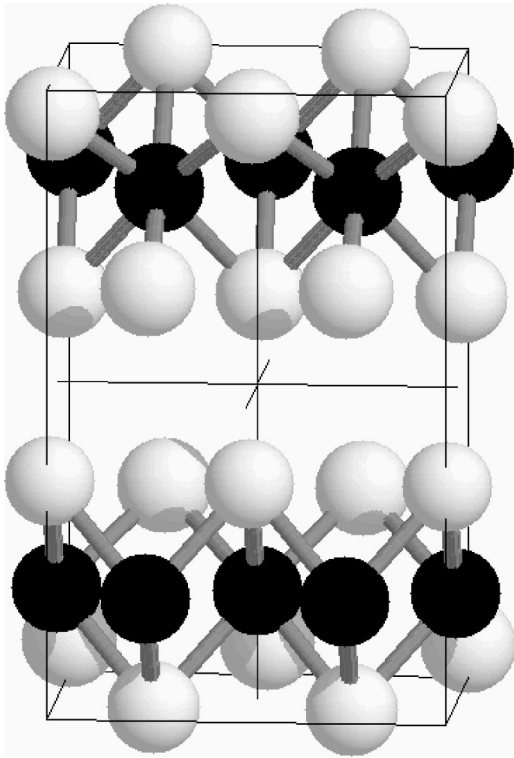


FIG. 1. Crystal structure of Td-WTe₂. Tungsten and tellurium atoms are printed in black and gray, respectively.

strong distortions. Their deviation from ideal octahedral geometry is accompanied by considerable shifts of the tungsten atoms away from the center of the octahedra in order to form pairs due to strong intermetallic bonding.

Specifically, the tungsten atom is shifted 0.95 Å horizontally from the center of the unit cell and 0.21 Å vertically relative to the center of the octahedron. As a result, every second row of W atoms pair, in order to form zigzagged, slightly buckled chains. As a consequence, the tellurium atom layers become corrugated, i.e., alternating rows of tellurium atoms are vertically displaced by 0.61–0.62 Å.^{8–11} The buckling allows the metal atoms in adjacent octahedra to approach each other with a resulting metal distance of only 2.86 Å. Each metal atom, therefore, has eight neighbors: six tellurium atoms and two metal atoms, because the metal atom neighbors are about the same distance from each other as the six tellurium atoms. The off-center position of the tungsten atoms together with the buckling of the tellurium layers gives the structure a definite ribbonlike aspect and is presumably responsible for the rodlike appearance of the Td-WTe₂ crystals instead of the flat appearance usually associated with layered compounds.

The stacking of one layer upon another is governed by the buckling of the layers so that adjacent layers are keyed together by an association of ripples and troughs. This gives rise to the 180° rotation of adjacent sandwiches and leads to the larger simple orthorhombic unit cell with four formula units. The space group is *Pnm*2₁. Cell dimensions, as measured on precession photographs,⁷ are $a = 6.282$ Å, $b = 3.496$ Å (both in plane), and $c = 14.07$ Å (perpendicular to the layers).

Under the assumption that the bonding between tungsten and tellurium is solely ionic (ionic limit) the electronic struc-

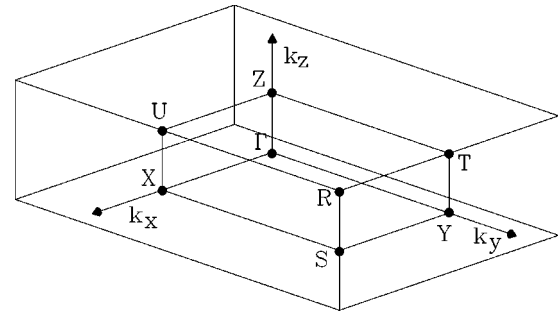


FIG. 2. Brillouin zone of the simple orthorhombic lattice.

ture of Td-WTe₂ should consist of fully occupied Te 5*p* states, which form extended valence bands, while the W 5*d* states possess two electrons. From the nearly octahedral crystal field at the tungsten sites we expect the 5*d* states to separate into the threefold *t*_{2*g*} manifold and the twofold *e*_g manifold. Due to the larger overlap with the ligand 5*p* orbitals, the latter states exhibit considerable bonding-antibonding splitting, while the *t*_{2*g*} bands reveal an almost nonbonding character.

III. BAND STRUCTURE CALCULATIONS

The calculations are based on density-functional theory (DFT) and the local-density approximation (LDA).^{12,13} We employ the ASW method¹⁴ in its scalar-relativistic implementation (see Refs. 15–17 for more recent descriptions). This method has already successfully been applied to the neighboring LTMD's TaS₂,¹⁸ TiTe₂.^{19,20} Since the ASW method uses the atomic sphere approximation,²¹ we had to insert so-called empty spheres into the open crystal structure of Td-WTe₂. These empty spheres are pseudoatoms without a nucleus, which are used to model the correct shape of the crystal potential in large voids. In order to minimize the sphere overlap, we have recently developed an algorithm,²² which solves the problem of finding optimal empty sphere positions as well as radii of all spheres automatically. By inserting 18 empty spheres into the simple orthorhombic unit cell of Td-WTe₂ we kept the linear overlap of any two physical spheres below 20%, and the overlap of any pair of physical and empty spheres below 27%.

Self-consistency was achieved by employing an efficient algorithm for convergence acceleration.²³ The Brillouin-zone sampling was done using an increased number of **k** points ranging from 54 to 6750 points within the irreducible wedge of the simple orthorhombic Brillouin zone shown in Fig. 2. This way we were able to ensure convergence of our results with respect to the fineness of the **k**-space grid.

Figure 3 shows the calculated band structure along various high-symmetry directions in the Brillouin zone (see Fig. 2). The corresponding W 5*d* and Te 5*p* partial density-of-states (DOS) are displayed in Fig. 4.

Except for the Te 5*d* states, which give rise to a small contribution above 1.5 eV, all other states play only a negligible role in the energy interval shown.

In the band structure a strong anisotropy of the band dispersions is observed. In particular, the very small dispersion parallel to Γ -Z is contrasted with large dispersions perpendicular to this direction reflecting the quasi-two-dimensional

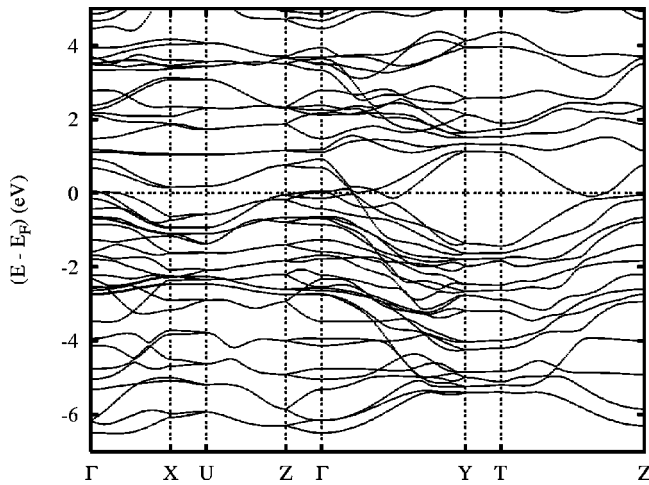


FIG. 3. Calculated electronic structure of Td-WTe₂. Here and in the following figures energies are given relative to the Fermi energy E_F .

nature of the layer compound. While the dispersion is larger for the occupied bands, the \mathbf{k} dependence is reduced above E_F , where single well separated bands can be identified. Due to this fact, and since most of the occupied bands have their maximum at or just below E_F (at Γ and Z) only few bands cross the Fermi energy, which gives a first clue to the observed low conductivity. In the total DOS this leads to a distinct minimum at E_F ; the still finite contribution there results from the two lowest unoccupied bands at Γ , which bend downward along the lines Γ -X and especially Γ -Y. Along the latter line these bands cross the Fermi energy and reach the Y point at about -1.6 eV. Although the bandwidth of about 2.5 eV is reminiscent of a typical metal, the low density-of-states at E_F resulting from the small number of strongly dispersing partially occupied bands, however, favors interpretation in terms of a semimetal rather than a metal.

The striking similarity of the W 5d and Te 5p contributions to the density-of-states in the whole energy range from -6.5 to about 4 eV, as displayed in Fig. 4, points to the strong covalent mixing of these states, which, like the strong

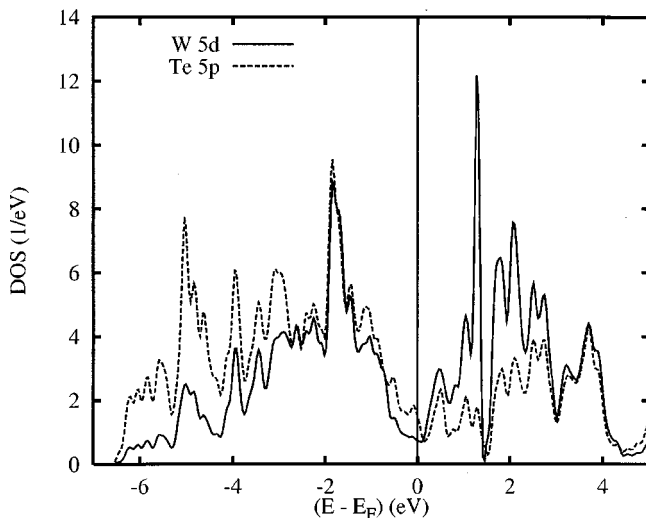


FIG. 4. Partial W 5d and Te 5p density-of-states of Td-WTe₂.

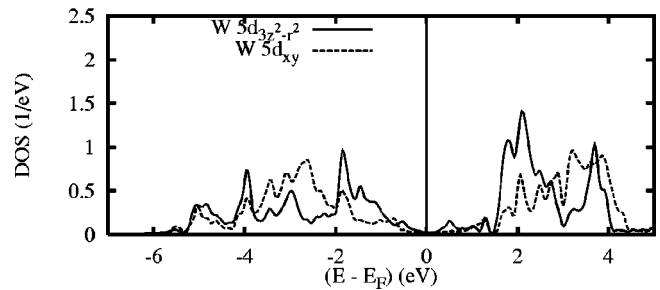
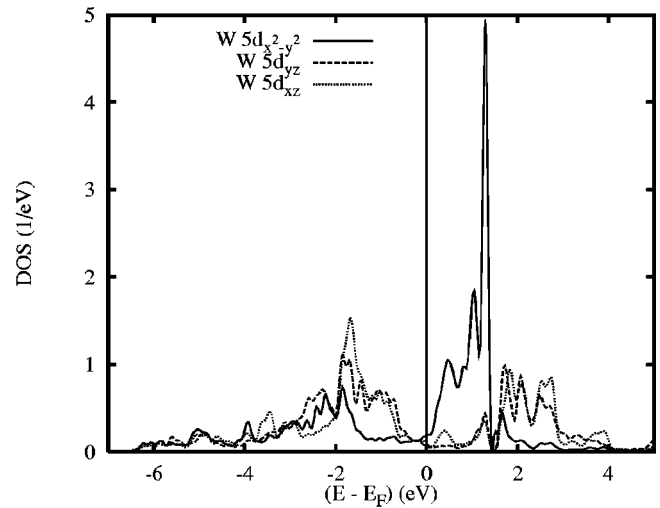


FIG. 5. Partial W 5d t_{2g} and e_g density-of-states. Selection of orbitals is relative to the local rotated reference frame (see text).

dispersion of the bands, results from their large overlap. Such a strong covalency was likewise observed in additional calculations for both hypothetical 1T-WTe₂ and 2H-WTe₂.²⁴ In contrast to the 1T polytype, however, distortion of the WTe₆ octahedra in the Td structure destroys the clear separation of the W 5d t_{2g} and e_g states. The partial DOS corresponding to the single 5d components are shown in Fig. 5, where we used a local rotated reference frame with the Cartesian axes adjusted to the local octahedron. Note, however, that due to an additional rotation by 45° about the z axis of the octahedron, the x and y Cartesian axes make an angle of 45° with the equatorial W-Te bonds. As a consequence, the $d_{x^2-y^2}$ and d_{xy} are exchanged and belong to the t_{2g} and e_g manifold, respectively. In Td-WTe₂, the symmetry of the d_{xy} and $d_{3z^2-r^2}$ orbitals as well as of the $d_{x^2-y^2}$, d_{xz} and d_{yz} orbitals is broken and the latter states experience some σ bonding due to the shift of the W atoms away from the centers of the octahedra. As a consequence, the t_{2g} derived states display considerable splitting between bonding and antibonding states, which are found below and above E_F , respectively, and leave the DOS minimum at the Fermi energy. According to Fig. 5, the bonding-antibonding splitting is larger for the d_{xz} and d_{yz} orbitals than for the $d_{x^2-y^2}$ orbitals. For this reason, the latter states dominate in the energy window ranging from E_F to 1.5 eV above. Just below E_F , the electronic structure changes from being rather isotropic to almost exclusively $d_{x^2-y^2}$ -like.

In order to lay ground for the subsequent detailed comparison of the calculated electronic structure with the angle-resolved photoemission data we next turn back to a discus-

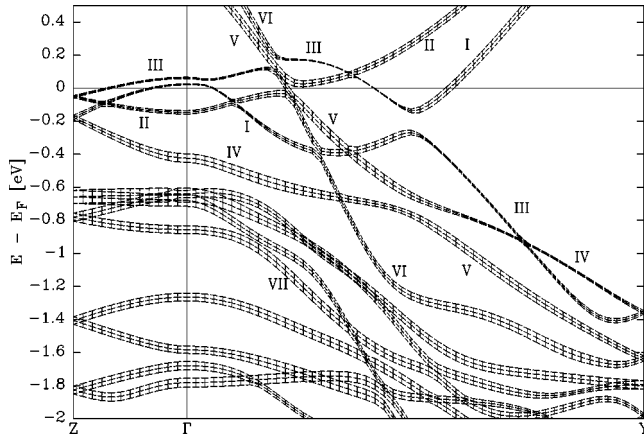


FIG. 6. Weighted electronic bands. The width of the bars given with each band indicates the contribution from the W $5d$ orbitals.

sion of the bands. To this end we complement the band structure given in Fig. 3 with Figs. 6 and 7.

In these figures the calculated bands are displayed in a special representation, where the width of the bars given with each band is a measure of the contribution from either the W $5d$ or the Te $5p$ orbitals. In addition, we have limited the representation to only a small energy window about the Fermi energy as well as to the symmetry lines Γ - Y and Γ - Z .

Again, we observe in Figs. 6 and 7 the pronounced quasi-two-dimensionality of the electronic structure. The only small dispersion along the line Γ - Z is contrasted with rather broad bands along the line Γ - Y . Furthermore, from Figs. 6 and 7 the electronic states can be grouped in two different categories: Bands, which are below -0.5 eV at Γ and Z comprise W $5d$ and Te $5p$ contributions to a similar degree, whereas the higher-lying bands, although likewise being of somewhat mixed character, experience considerable variation of the band characters across the Brillouin zone. This is particularly visible for bands I and II, which, while bending upward, increase their W $5d$ weight at the expense of the Te $5p$ character. This holds especially after these bands have crossed the Fermi level at about $0.6\Gamma Y$ and $0.2\Gamma Y$, respectively. In accordance with the above discussion of the partial density-of-states a more detailed analysis of the band structure showed that above E_F both bands are almost exclusively

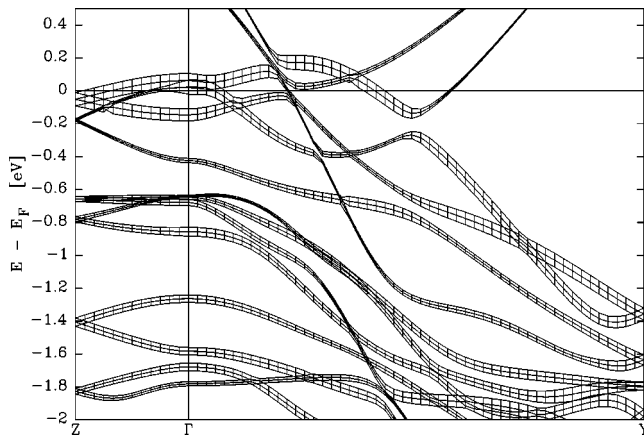


FIG. 7. Weighted electronic bands. The width of the bars given with each band indicates the contribution from the Te $5p$ orbitals.

of $d_{x^2-y^2}$ character. A completely different behavior is displayed by bands III and IV, which, although being degenerate with bands I and II at the Z point, have a reversed curvature and thus end at 1.4 eV below the Fermi energy at the Y point. These two bands are of dominant Te $5p$ character throughout their way along Z - Γ - Y (band III) or change from W $5d$ - to Te $5p$ -dominated (band IV). From the previous discussion we arrive at the picture of two mainly unoccupied W $5d$ -like bands (bands I and II), which overlap with two predominantly occupied Te $5p$ -like bands (bands III and IV) with an overlap region of approximately 0.55 eV. Taking bands I to IV alone we would thus end up with a classical semimetal.

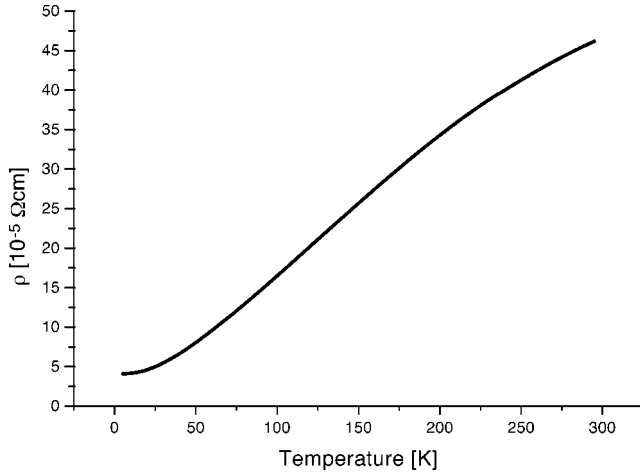
However, the just sketched clear picture is undermined by bands V and VI, which start 0.7 and 0.9 eV above E_F at Γ , respectively, dip below E_F at about $0.2\Gamma Y$, and disperse downward until they reach the Y point at -1.6 eV. With decreasing energy, both bands change from predominantly W $5d$ to Te $5p$ character. These bands can be well classified as metallic. To conclude, we thus arrive at a combined semimetallic and metallic behavior for Td-WTe₂.

IV. EXPERIMENTAL DETAILS

The angle-resolved photoemission measurements were performed at the $3m$ normal-incidence-monochromator beamline HONORMI, at the Hamburg Synchrotron Radiation Laboratory (HASYLAB), which covers a photon energy range of $9 \text{ eV} < h\nu < 27 \text{ eV}$. The spectrometer consists of a 180° spherical energy analyzer mounted on a goniometer, which can be rotated around two independent axes. For the spectra represented here, an overall energy resolution of $80 \text{ meV} \leq \Delta E \leq 100 \text{ meV}$ and an angular resolution of $\Delta\theta < 0.9^\circ$ were achieved, while the absolute accuracy of the emission angle was 0.1° . The position of the Fermi edge of platinum was used as a reference for the binding energy of the spectra.

The Td-WTe₂ single crystals were grown using the chemical vapor transport method in horizontal reactors with bromine as the transport gas. The quality of the crystals was characterized by secondary ion mass spectroscopy (SIMS) in order to examine the chemical purity. Structural and electrical properties were analyzed using Laue x-ray diffraction as well as temperature-dependent transport measurements. The Laue diffraction patterns were also used to determine the high-symmetry directions in reciprocal space. The final sample orientation for the photoemission measurements was precisely adjusted from the symmetry of the photoemission spectra with respect to equivalent high-symmetry directions. Because of the high quality of the samples and the high resolution of the experimental setup, an orientation of the samples with an accuracy of 0.1° could be achieved.

Clean Td-WTe₂ surfaces were prepared *in situ* by cleaving the crystals along their weakly bonded sandwich layers. Cleavage and photoemission measurements were made at a base pressure of 3×10^{-10} mbar at room temperature. The complete photoemission data set presented in Sec. VI was obtained from one sample within a 17 h time frame. There was no observable time dependence in the spectra due to adsorbed residual gas or effects such as band bending. The

FIG. 8. Temperature-dependent in-plane resistivity of Td-WTe₂.

results presented here have been reproduced on a total of four samples.

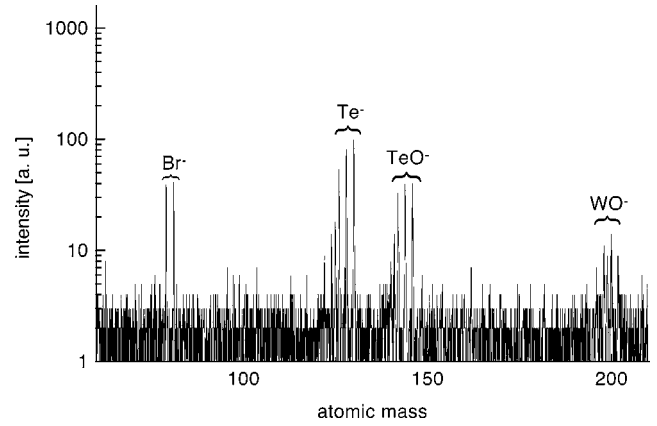
V. CHARACTERIZATION

The crystal structure of WTe₂ has been investigated using Laue x-ray diffraction. While all crystals clearly showed a twofold rotation axis, no indication for the 1T- or 2H-polytype were found.

The metallic behavior of Td-WTe₂, as proposed by Dawson and Bullett,⁴ as well as from our own theoretical work, was checked using transport measurements. This is easily seen in Fig. 8 where, with decreasing temperature, the in-plane resistivity reaches a residual value, which can be determined to be $\varrho = 4.1 \times 10^{-5} \Omega \text{ cm}$ at $T = 1.9 \text{ K}$. With increasing temperature, the resistivity rises nearly linearly between 20 K and 300 K. At $T = 273 \text{ K}$ the resistivity can be determined to be $\varrho = 4.4 \times 10^{-4} \Omega \text{ cm}$. Similar results have been observed by Brixner⁵ as well as by Kabashima⁶ who employed a semimetallic band structure including three charge carriers. Above room-temperature excitations from a lower to the upper *d* band cause decreasing resistivity similar to that caused by a degenerate semiconductor.

The chemical composition and purity of the samples was analyzed using SIMS. All spectra have been recorded for O₂⁺ primary ions. Positive and negative ions can be detected as secondary ions in order to study the contamination with electropositive or electronegative materials. Spectra recorded for positive secondary ions did not show any significant contamination with electropositive materials such as metals. The search for electronegative substances revealed the transport agent bromine as can be seen in Fig. 9.

Bromine was obviously incorporated in the crystals by the chemical vapor transport growing process. Energy dispersive x-ray (EDX) measurements show the bromine content lying below the detection limit ($5 \times 10^{19} \text{ cm}^{-3}$). Such a small density would not be expected to influence the electronic properties of a metallic host crystal significantly, e.g., more than the self-intercalation effect commonly present in layered crystals. As mentioned above, the secondary ion emission probability of negatively charged tungsten atoms is rather low. Tungsten is therefore not visible in this spectrum.

FIG. 9. SIMS analysis of Td-WTe₂ grown with bromine.

VI. ANGLE-RESOLVED PHOTOEMISSION

Spectra shown in this section are energy distribution curves (EDC) with either the electron emission angle ϑ or the photon energy $h\nu$ as a parameter. Through the variation of the polar angle ϑ , the components of the photoelectron wave-vector parallel and perpendicular to the layers change. The momentum component parallel to the surface can be obtained directly from the kinetic energy and the emission angle ϑ as

$$k_{\parallel} = \sqrt{\frac{2m_e}{\hbar^2} E_{kin} \sin^2 \vartheta}. \quad (1)$$

This relationship results from the momentum conservation parallel to the surface when a photoelectron leaves the crystal. In contrast, the wave-vector component perpendicular to the surface is not conserved due to the broken translational symmetry. Assuming direct transitions into free-electronlike final states, this component is determined by

$$k_{\perp} = \sqrt{\frac{2m_e}{\hbar^2} (E_{kin} \cos^2 \vartheta + V_0)}, \quad (2)$$

where V_0 is the inner potential with respect to the vacuum level. The experimental band structure $E_B(\mathbf{k})$ follows from the energy conservation,

$$E_B = E_{kin} - h\nu + \Phi, \quad (3)$$

where Φ is the work function of the sample. On this basis, it is possible to measure the dispersion of the valence bands in various directions in reciprocal space after orienting the sample. However, in a certain direction parallel to the layers, one is actually not scanning along this direction but rather along a parabolic path in three dimensional space due to k_{\perp} dependence. For quasi-two-dimensional materials like the layered transition-metal dichalcogenides, however, one would also usually expect the electronic band structure not to depend strongly on k_{\perp} . This will be demonstrated for WTe₂ in the following section.

A. Dispersion perpendicular to the layers

Equation (1) implies that measuring photoemission spectra in normal emission ($\vartheta = 0^\circ$) gives $k_{\parallel} = 0$. The wave-

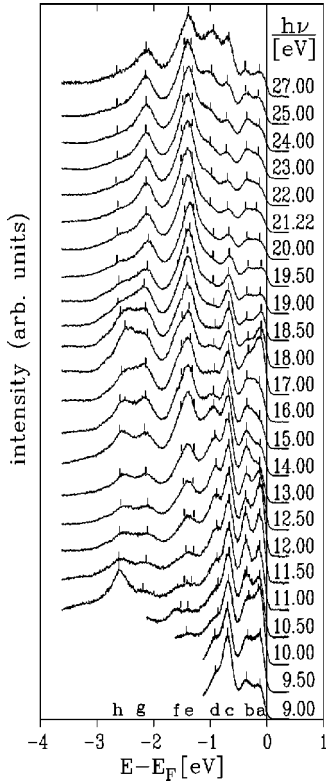


FIG. 10. Energy distribution curves of Td-WTe₂ along Γ -Z.

vector component perpendicular to the planes k_{\perp} depends on the kinetic energy of the photoelectrons according to Eq. (2). Because the kinetic energies of the photoelectrons vary with photon energy, the Brillouin zone can be scanned along the line Γ -Z. A selection of valence-band spectra for photon energies between $h\nu = 9$ eV and 27 eV is shown in Fig. 10.

The binding-energy region (down to -4 eV) was chosen to provide more detail in the upper valence band. The emission maxima and structures are labeled by small characters in Fig. 10. As is obvious from the spectra series, the dependence on photon energy (k_{\perp}) is quite small except for some intensity modulations due to variations of the transition matrix element. This directly reflects the quasi-two-dimensional electronic character of Td-WTe₂, similar to that of the 1T- or 2H-type layered transition-metal dichalcogenides, which display no octahedral distortion. However, such a pronounced two dimensionality of the band structure is remarkable, even for the layered TMDC's.

To find out which k_{\perp} values have to be attributed to the emission features, their weak dispersions have to be investigated in more detail. In general, three different methods of determining the inner potential V_0 are employed. It may be (i) adjusted to an optimal agreement between theoretical and experimental band structures, (ii) determined from the muffin-tin zero, or (iii) evaluated from symmetry considerations of the experimental $E_B(k_{\perp})$ curves.³⁰ In the present paper, all three criteria are used. To this end, the symmetries of the most dispersive bands in the k_{\perp} series are analyzed (see Fig. 10). Intensity criteria are also used. From the resulting V_0 , the experimental band structure $E_B(k_{\perp})$ can be deduced, which is compared to the theoretical band structure.

The bands “e” and “f” are the most dispersive structures in the direction Γ -Z. These states periodically approach each

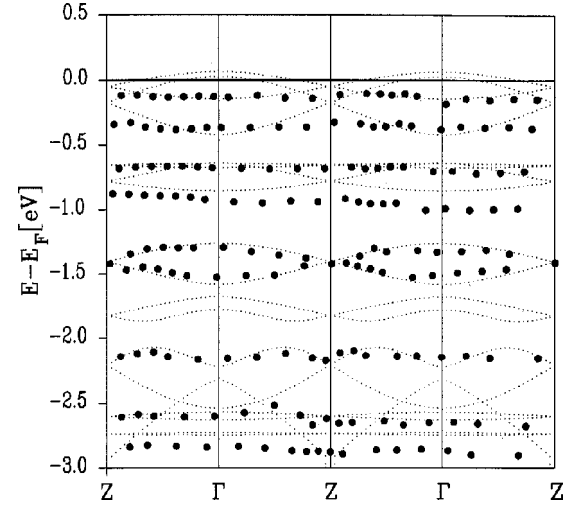


FIG. 11. Comparison of measured and calculated band structure along Γ -Z.

other and separate again.³¹ Keeping in mind the periodicity of these bands, and assuming a reasonable value for V_0 , the Z point is found to lie at about 18 eV photon energy. Consequently, states excited with $h\nu = 22$ eV stem from the direct vicinity of the Γ point. For the uppermost band “a,” the Z point and the Γ point are found for 17 eV and 21.22 eV photon energy. The V_0 thus obtained is 11.5 eV. The theoretically derived inner potential refers to the muffin-tin zero (MTZ) and can be calculated from

$$V_0 = \Phi + E_F - \text{MTZ}. \quad (4)$$

With the experimental work function of $\Phi = 4.7$ eV, we obtain an inner potential of 11.6 eV, which is in close agreement with the experimental value. Using the experimental value for the direction Γ -Z we arrive at the band structure displayed in Fig. 11.

For the most dispersive bands “e” and “f” in the k_{\perp} series, the agreement between the experimental and theoretical band structure is very good. Thus, all three criteria for determining the inner potential lead independently to the same value for V_0 .

It is obvious when analyzing the experimental and theoretical band structures in Fig. 11 that a large number of the manifold of theoretical bands are experimentally confirmed. In addition, the band energies of experiment and theory agree well. This is valid for both the higher and lower range of binding energies. The binding energies of the bands differ by a maximum of 100 meV. In addition, the bands are qualitatively well described by the theory. Apart from the very good agreement of “e” and “f,” the dispersion of the bands “g,” “h,” and “h'” agree well at binding energies higher than -2 eV. For band “g,” in particular, the periodicity of the Brillouin zone can be observed in agreement with the theory.

A further analysis of Fig. 11 shows that the calculation predicts more bands than were experimentally resolved. This is valid both for the range near E_F and that below -1.5 eV binding energy. This explains the seeming overestimation of the dispersions by the theory, especially for

bands “*c*” and “*d*.” The range of lower binding energies with the bands “*a*” and “*b*” is particularly affected.

In the following discussion, both the orbital character and the dispersion of the individual bands will be addressed. At this point it should be emphasized that results from the calculated band structure are used in this and in the following sections in the analysis of the orbital character of the experimental bands. Weighted, \mathbf{k} -resolved band structures are used in order to assign single band symmetries. These calculations were not always represented in Sec. III. The bands “*a*” and “*b*” are of special interest since they determine the low energy properties of WTe_2 .

Due to the good agreement of band energies it is possible to assign band “*b*” definitely to the LDA band IV in Fig. 6. The analysis of the orbital character as given in Figs. 6 and 7 allows us to attribute a W $5d$ and Te $5p$ character to band “*b*.” In this energy region the tungsten contributions derive mainly from the $d_{3z^2-r^2}$ states. Note that in this context, the labelling of the orbitals refers to the global reference frame with the Cartesian axes adjusted to the primitive translations of the lattice. Starting from the Γ point up to half the $\bar{\Gamma}Z$ distance, band “*b*” is well described by the theory except for minor deviations. However, the calculations show that the closer one gets to the Brillouin-zone boundary, the more marked the three-dimensional electronic behavior becomes, more than was in fact experimentally observed.

The same applies to peak “*a*.” Apparently, the course of band “*a*” is experimentally only slightly k_{\perp} dependent. However, detailed analysis shows a slight dispersion of structure “*a*” to higher-binding energies between 13 eV to 17 eV photon energy. Apparently band “*a*” disperses symmetrically about the Z point. In particular, at the Brillouin-zone boundary the calculations show clearer dispersion to lower-binding energies, which cannot be observed in the EDC’s. It is to be assumed that these discrepancies can be attributed to the probability that there are more bands in the range of lower-binding energies than are experimentally resolved. Up to a binding energy of -0.5 eV, the calculations show four bands, two of which remain unoccupied over large sections of the Brillouin zone. With increasing approximation to the Z point these states should be occupied, and therefore be observable by means of photoemission spectroscopy. A clear assignment of band “*a*” to a definite calculated state and therefore to a definite orbital symmetry in this respect is difficult. The weighted energy-band structures in Figs. 6 and 7 point, however, to a Te $5p$ character in this binding energy range.

The almost two-dimensional electronic character measured near the Fermi energy indicates apparently, that bands “*a*” and “*b*” could be occupied over the whole of the Brillouin zone. In this respect the Fermi-level crossings predicted by the theory cannot be directly observed in the EDC’s. A more detailed analysis of the low-energy range on a smaller energy scale shows, however, that band “*a*,” in particular, could show a Fermi-level crossing at photon energies between 17 eV and 19.5 eV. Further discussion of this binding energy range can be found in Sec. VII.

The reason for the experimentally unresolved electronic fine structure, particularly near E_F , lies in the broadening of the peak widths due to the chosen temperature. Taking monochromator and energy analyzer resolution into consid-

eration, the overall energy resolution is about $\Delta E = 140$ meV. Especially the LDA bands I to III, which have to be assigned to band “*a*” (see Fig. 6), differ in binding energy by at most 60 meV and hence are not separated experimentally. Particularly considering spin-orbit interactions, this could lead to interferences that possibly obscure a clear Fermi-level crossing, electronic fine structure, and k_{\perp} dependences.³² This problem exists also at higher-binding energies for the bands “*c*” and “*h*,” which do not demonstrate dispersion. Their theoretical fine structured counterparts are not resolved experimentally.

According to the analysis of the band structure, with respect to the orbital character, as given in Figs. 6 and 7, the bands labeled “*c*” and “*d*” in Fig. 10, which range from 0.7 eV to 0.9 eV below E_F , arise from similar contributions from the W $5d$ and Te $5p$ states. From a more detailed theoretical analysis, we are able to assign the $5d$ contributions almost exclusively to the $5d_{3z^2-r^2}$ (band “*d*”) and $5d_{yz}$ states (band “*c*”). In Td- WTe_2 the W $5d_{3z^2-r^2}$ -dominated band is thus lying at higher-binding energies than in the case of WSe_2 .²⁵⁻²⁹

Between -1.6 eV and -1.8 eV there are two LDA bands that cannot be observed experimentally. A comparison with the EDC spectra in Fig. 10 shows a clear minimum of intensity at this binding energy. This discrepancy between experiment and theory can be attributed to final-state effects. In the range of the final states at 19.4 eV above E_F the theory shows at the Γ point an 0.6 eV wide gap. With increasing approximation to the Z point, the size of this gap increases. Neglecting correlation effects, this lack of final states could explain why the calculated bands cannot be observed experimentally along Γ -Z. It is expected that it will also be possible to observe this final-state effect along the parallel measuring direction Γ -X.

At higher binding energies the corresponding final states lie outside of this gap and agreement between theory and experiment is restored. Due to the good agreement, it is possible to assign the bands “*g*,” “*h*,” and “*h'*” to almost equal contributions from the Te $5p$ and W $5d$ states.

To summarize, it is convenient to divide this spectra series into three different regions, namely, (i) the upper chalcogen dominated $5p$ -derived conduction band “*a*” (region A), (ii) the mainly metal $5d$ -derived bands “*b*” to “*f*” (region B), and (iii) the deep Te $5p$ bands “*g*,” “*h*,” and “*h'*,” which are hybridized with W $5d$ states (region C). All these regions consist of almost flat bands along Γ -Z. Thus, in comparison to layered systems with more regular metal-chalcogen units the three dimensionality of the electronic properties is very reduced in Td- WTe_2 .

Generally, from the comparison in Fig. 11, we find good agreement between experiment and theory. Where deviations are observed, they can be well understood as due to final-state effects or to thermal broadening of the photoemission features. Going beyond the assignment of binding-energy ranges to definite atom orbitals, it is possible to draw the conclusion that the approximation of parabolic final states seems suitable for Td- WTe_2 in direction Γ -Z. In particular, the determination of the high-symmetry points Γ and Z, which is important for the following parallel measuring di-

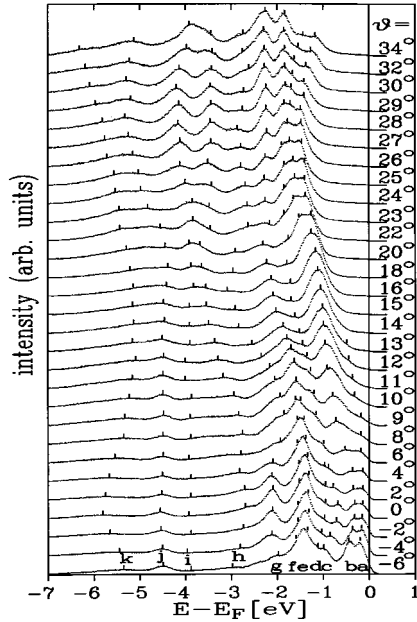


FIG. 12. Energy distribution curves of Td-WTe₂ along Γ -Y (Z-T).

rections, was successful as bands “e,” “f,” and “g” especially demonstrate. The k_{\perp} uncertainty at these points seems to be minimal.

B. Dispersion parallel to the layers

The valence-band dispersions of Td-WTe₂ along the high-symmetry directions Γ -Y (Z-T) and Γ -X (Z-U) are represented in Figs. 12 and 13, respectively. In the discussion of the bands along these high-symmetry directions we will concentrate especially on the orbital character of the bands and semimetallic behavior. The samples were irradiated by synchrotron radiation of photon energy $h\nu = 21.22$ eV. As illus-

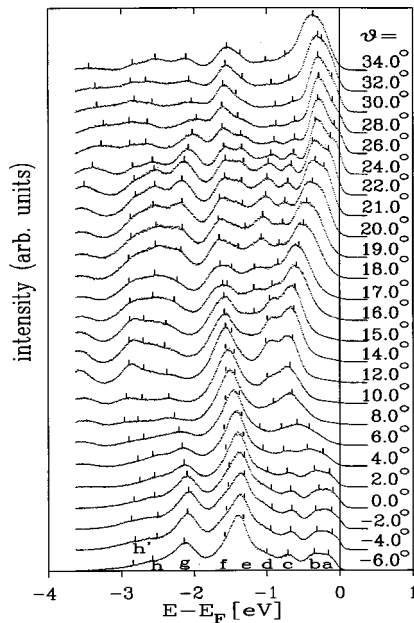


FIG. 13. Energy distribution curves of Td-WTe₂ along Γ -X (Z-U).

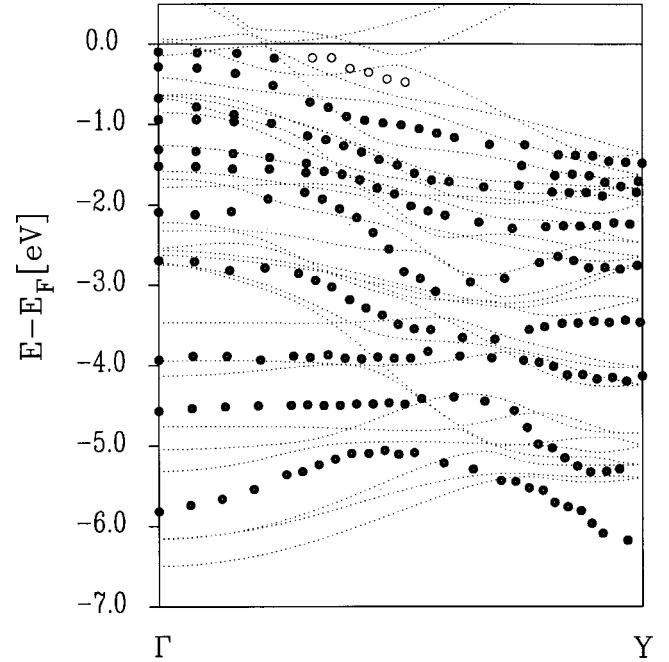


FIG. 14. Energy-band structure of Td-WTe₂ along Γ -Y (Z-T).

trated above, the electronic states near the Fermi level excited by this energy are located in the direct vicinity of the Γ point in normal emission.

In the direction Γ -Y (Z-T), 11 bands are identified between -7 eV and the Fermi level. Again they are marked with lower-case characters. The experimental band structure $E_B(k_{\parallel})$ derived from the EDC’s of Fig. 12 is displayed and compared to the theoretical band structure along the line Γ -Y in Fig. 14.

As can be seen in this figure the number of the LDA bands is very large: 30 calculated bands are to be found in this direction. The resulting density-of-states is very high compared with transition-metal dichalcogenides in the 1T structure. Therefore, as already mentioned in Sec. VI A, not all LDA dispersions are experimentally resolved. Correspondingly, clear assignments of experimental to calculated bands are difficult. This applies to both directions Γ -Y and Γ -X, oriented parallel to the layers.

Again we can identify the three regions A, B, and C, as defined in the previous analysis of the spectra, measured along the direction Γ -Z. A further series of bands, emissions “i” to “k,” appears in the energy range between -6.0 eV and -4.0 eV, which was not included in Figs. 10 and 11. From the band calculations, in particular from the partial DOS shown in Fig. 4, these emissions can be attributed mainly to Te 5p states. The corresponding energy range is assigned as region D. States in this region represent the deep chalcogen states. Dispersions of similar magnitude are also observed in undistorted layered systems. Their energetic position is in accordance with the simple band model of Wilson and Yoffe.³ However, we can still observe admixture from the W 5d states in Fig. 4, which arises from similar contributions from all the five 5d states. In this binding energy range the experimental bands are described qualitatively rather than quantitatively by the theory. For “k” and “j,” qualitatively similar LDA dispersions can be found, however, which have band energies that are approximately 0.5

eV too high. The measured band energies indicate that in normal emission the actual k_{\perp} for “ k ” corresponds to the Z point. However, band “ k ” in particular, reveals in the k_{\perp} direction a dispersion that cannot be ignored, as the 0.5 eV difference between the points Γ and Z shows. Since the trajectory scanned experimentally in \mathbf{k} space deviates emission-angle dependently from the ΓX line, the associated k_{\perp} deviation leads to discrepancies between theory and experiment. Better agreement is found for band “ i ,” which shows less dispersion perpendicularly to the layers.

Increased admixture of tungsten orbitals characterizes the bands “ g ” and “ h .” In accordance with the classification of Sec. VI A these bands belong to region C . The states in this binding-energy range are described better by the theory both quantitatively and qualitatively.

The first emissions dominated by metal orbitals are bands “ e ” and “ f ,” which are attributed to region B . The $W 5d_{3z^2-r^2}$ dominated band “ d ,” which is found at -0.9 eV at the Γ point, disperses downwards to -1.9 eV at the Y point (see Fig. 14). Further analysis of the orbital weighted band structure shows that band “ b ” possesses mainly $W 5d_{3z^2-r^2}$ orbitals. Hence, the upper part of region B between -0.8 eV and -0.3 eV, shows a considerable admixture of $W 5d_{3z^2-r^2}$ states, the only exception being band “ c ,” which displays a predominantly $W 5d_{yz}$ character. Qualitatively the whole region is well described by the theory. As the measurements in the ΓZ direction show, the bands of regions C and B are distinctly two dimensional so that k_{\perp} uncertainties do not play any role.

Since the macroscopic electrical behavior of $Td-WTe_2$ is determined by the low-energy region, we concentrate in the following on the bands near the Fermi energy, in other words, bands “ a ” and “ b ” along the line $\Gamma-Y$ ($Z-T$), where these states display their strongest dispersion. This is illustrated in Fig. 17, which shows a small energy range near E_F .

For the emission spectrum at $\vartheta = -6^\circ$ one observes a double structure in the first 600 meV below E_F . Near the Γ point the topmost bands “ b ” and “ a ” approach each other to form one broad structure, and separate again in a double structure beyond the Γ point. For higher emission angles, “ a ” and “ b ” show a pronounced dispersion away from E_F . Additionally, the emission of band “ a ” loses weight until it finally vanishes at about $\vartheta = 13^\circ$ (see Fig. 12). Details concerning the low-energy region of WTe_2 will be discussed in Sec. VII.

The spectra for a second high-symmetry direction parallel to the layers, $\Gamma-X$ ($Z-U$), are shown in Fig. 13. This series is measured from one Γ point through the X point at $\vartheta = 14^\circ$ to the next Γ point at $\vartheta = 30^\circ$. The binding-energy region given here was chosen in such a way as to show the upper valence band down to -4 eV binding energy in more detail. The orbital character of the bands at the center of the Brillouin zone has already been discussed together with the ΓY direction. Similarly the ΓX direction exhibits three valence band regions due to the typical orbital character: the upper chalcogen dominated p -conduction band “ a ” (region A), the metal $5d$ derived bands “ b ” to “ f ” (region B), and finally the deep Te $5p$ -based bands “ g ,” “ h ,” and “ h' ” (region C).

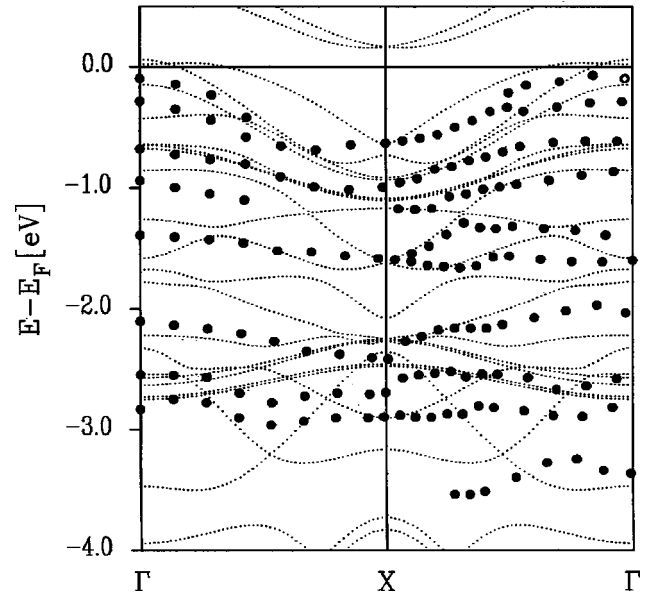


FIG. 15. Energy band structure of $Td-WTe_2$ along $\Gamma-X$ ($Z-U$) over the X point to the second Γ point.

According to this classification, bands between -2 and -4 eV binding energy are attributed to region C , i.e., essentially Te $5p$ states with some $W 5d$ admixture. Their qualitative dispersions are in good agreement with the calculations, as can be seen in Fig. 15. Here emission maximum “ h ” of region C consists of two peaks, assigned “ h ” and “ h' ” because of the better resolution. These bands are about 0.3 eV apart. This finding can be attributed to spin-orbit splitting, which has also been observed for the corresponding Te $5p$ band in $TiTe_2$.³² Spin-orbit coupling was not included in the LDA calculation, and is therefore not reproduced in the theoretical band structure. The measured band energy indicates that the actual k_{\perp} corresponds to some intermediate position along $\Gamma-Z$. The qualitative course of this band is better described in the ZU direction in the top plane of the Brillouin zone as can be seen in a comparison with the LDA band structure in Fig. 3. The same holds for band “ g ,” which starts in normal emission at -2.1 eV and disperses to the higher-binding energy of -2.4 eV at the $X(U)$ point.

Between -2 eV and -1.5 eV there are two LDA bands, which are not resolved experimentally. The EDC spectra in Fig. 15 show a clear minimum in intensity. Analogous to the measuring direction $\Gamma-Z$ in Sec. VI A, at 19.5 eV above E_F , there is a gap in the theoretical band structure in which there are no final states. Correspondingly the photoelectrons do not find any final state to couple on and are therefore not observable experimentally.

For regions A and B k_{\perp} uncertainties decrease when approaching E_F . The agreement between experiment and theory increases correspondingly. For the low-energy bands “ b ” and “ a ” one observes a considerably higher intensity at the second Γ point than at the first Γ point. Following the superimposed bands “ a ” and “ b ” at $\vartheta = 14^\circ$, the X point, their spectral weight increases continuously with increasing emission angles. The profile becomes more and more asymmetrical and for $\vartheta \geq 21^\circ$ a second maximum, band “ a ,” splits off, which disperses towards E_F . It reaches a minimal binding energy of 75 meV at $\vartheta = 26^\circ$. For even greater emis-

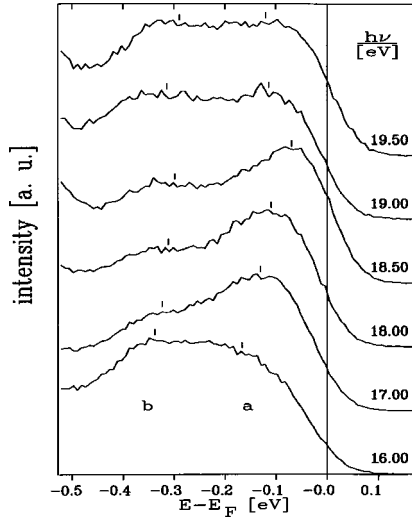


FIG. 16. Energy distribution curves of Td-WTe₂ along Γ -Z for small binding energies. The spectra show a discontinuous change in dispersion at $h\nu=18.5$ eV (see text).

sion angles again it loses spectral weight, possibly indicating a Fermi-level crossing. Obviously due to the higher intensity for these emission angles it is easier to investigate the behavior near E_F for the greater polar angles. Transforming the potential crossing point at 26° into the first Brillouin zone, it corresponds to $\vartheta=2^\circ$, i.e., 15% of the zone extension in direction Γ -X. This would be in close agreement with the theoretical result (see Fig. 15). A second hint for a Fermi-level crossing of the uppermost band ‘a’ near Γ is the clear appearance of a Fermi edge for emission angles of about 26° (see Fig. 13). However, there is a problem remaining, in that the theory proposes two bands at E_F near Γ (see Fig. 17) which are not resolved experimentally.

VII. DISCUSSION

The overriding features of the valence-band structure of Td-WTe₂ discussed in Sec. VI, show that the combined results of experiment and theory are in good agreement. On the other hand, some differences between theory and experiment exist, particularly at E_F and in principle due to the fact that the theoretically proposed fine structure of the band structure is not fully resolved experimentally. As it is this energy range that determines the transport properties and the electrical character of this material, we will discuss the behavior of band ‘a’ in more detail below.

Figure 16 shows spectra in direction Γ -Z near the Fermi energy for photon energies between 16 eV and 19.5 eV. All of the tick mark positions shown here result from fits with Gaussian profiles in which the Fermi Dirac distribution function was taken into account, in particular close to the Fermi energy.

Starting from 16 eV excitation energy, one can see that the emissions from band ‘a’ gain in spectral weight and decrease again from $h\nu=19$ eV. Furthermore, in contrast to Fig. 10, a marked continuous dispersion to lower binding energies can be observed. At $h\nu=16$ eV state ‘a’ has a binding energy of -170 meV. Up to 18.5 eV photon energy, ‘a’ disperses to its minimum binding energy of

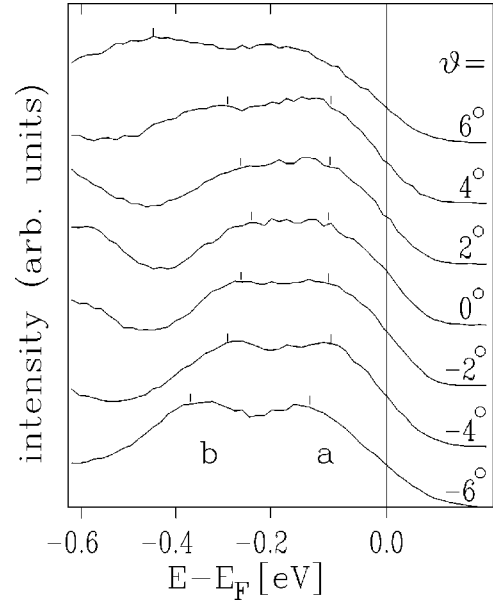


FIG. 17. Energy distribution curves of Td-WTe₂ along Γ -Y (Z-T) for small emission angles. The spectra show a marked drop in intensity at $\vartheta=4^\circ$ (see text).

-70 meV, whereby its full width at half maximum drops to 180 meV. This is the smallest value for all spectra in the measuring direction Γ -Z. At higher-photon energies of $h\nu=19$ eV, ‘a’ shows a marked dispersion back to higher-binding energies. As is also visible in Fig. 11, the change in dispersion is discontinuous. In addition, on going from $h\nu=18.5$ eV to $h\nu=19$ eV the peak intensity decreases drastically. In particular, the latter two observations hinder to interpret the behavior of band ‘a’ at $h\nu=18.5$ eV as a simple band maximum with the band remaining completely occupied in the whole range of photon energies given in Fig. 16. In contrast, the following two scenarios are possible. (i) There may be a crossing of band ‘a’ with another band ‘a’ at 18.5 eV photon energy, the details of which are beyond the experimental resolution. This would explain both the kink in dispersion and the drastic drop in intensity. (ii) However, the experimental observations could be likewise understood in terms of a Fermi-level crossing. Although both interpretations are in agreement with the band structure results (see Fig. 11), this second alternative is strongly supported by a detailed analysis of the half width at half maximum of band ‘a,’ which displays the aforementioned distinct minimum at $h\nu=18.5$ eV. Referring to the \mathbf{k} -space position this crossing is in good agreement with the calculated band structure (band III). The measured and calculated Fermi vectors agree within 0.03 \AA^{-1} . However, the overall dispersion of the photoemission peak appears quantitatively reduced by a factor of 0.4 relative to the LDA results.

From a further comparison with the electronic structure calculations, a second conduction band crossing the Fermi level at $h\nu=19.5$ eV (see Fig. 11) can be predicted. This crossing cannot be observed in Fig. 16. However, there is no increase in the spectral weight and no clear dispersion. A clear statement in respect of a second crossing cannot be experimentally proven because the double structures of states ‘a’ and ‘b’ develop into a broad structure at this photon energy. Within this structure a clear determina-

tion of the peak positions is not possible.

Spin-orbit interactions, which had not been taken into consideration in the LDA calculations can, however, lead to only one crossing through the Fermi level in the measuring direction Γ -Z. In particular the LDA band III (see Fig. 6) could split because of the spin-orbit interaction and as a result be completely unoccupied. For the Te $5p$ derived bands, the spin-orbit splitting at Td-WTe₂ could be determined to 0.3 eV in accordance with TiTe₂.³²

Figure 17 shows spectra along Γ -Y (Z-T) near E_F for small emission angles. Noticeable for angles up to $\vartheta = \pm 4^\circ$ is that the intensity of band “a” increases slightly and the binding energy reaches a minimum of 90 meV at $\vartheta = 4^\circ$. Band “b” shows on either side of the Γ point ($\vartheta \neq 0^\circ$) a clear dispersion to higher-binding energies. As is also visible in Fig. 14, the change in dispersion of band “a” on going from $\vartheta = 4^\circ$ to $\vartheta = 6^\circ$, is discontinuous. Additionally, the peak intensity decreases drastically. These experimental observations have already been made at $h\nu = 18.5$ eV along Γ -Z. In particular, the discontinuity hinders to interpret the behavior of band “a” as a simple dispersion back to higher-binding energies. As also can be seen in Fig. 14, there may be two metallic conduction bands, labeled V and VI in Fig. 6, crossing the Fermi energy and band “a.” In this case the peak intensity of band “a” should slightly increase instead of decrease. Therefore, the experimental observations point to a Fermi-level crossing of band “a” at $\vartheta = 4^\circ$ along the Γ Y line. The position of this possible crossing is in agreement with the calculated band structure as can be seen in Fig. 14.

The theory proposes six bands crossing the Fermi energy along the Γ Y direction. Near the Γ point one would expect to observe two crossings of band I and II at $\vartheta = 2^\circ$ and $\vartheta = 5^\circ$ (see Figs. 6 and 14). One of these crossings may be that of the experimentally indicated band “a.” Additionally, the calculated band structure implies that peak “a” consists of two states near the Fermi level within the low-energy region up to a binding energy of -0.2 eV, namely, bands I and II. Indeed, structure “a” is relatively broad for all spectra between the Γ point and $\vartheta = 13^\circ$. In particular, it can be assumed that these broad structures contain additional Fermi-level crossings. Furthermore, the LDA calculation yields a drastic character change of band II from predominantly Te $5p$ -like to essentially W $5d$ near and above the Fermi energy. Together with the unresolved states, this can lead to an alteration of the transition probabilities from this band, and may conceal a Fermi-level crossing. The remaining four Fermi-level crossings originate on the one hand from two crossings of the two metallic bands V and VI, which are difficult to separate, and on the other hand from bands I and III at 0.6Γ Y and 0.4Γ Y, respectively. These bands are exceptionally dispersive and are not observed experimentally. Because of the resulting low density-of-states at E_F , these dispersions are difficult to resolve in photoemission spectroscopy. Photoemission measurements at highest resolution and low-temperatures finally will provide information about the low energy range.

With respect to the transport properties of Td-WTe₂, the orbital weighted LDA band structure offers two possible explanations: one is based on semimetallic and the other on

metallic behavior: The metallic behavior results from the very dispersive bands V and VI (see Fig. 6). The semimetallic behavior should result from several band overlaps, the p/d overlap of the W $5d$ bands I and II with the Te $5p$ bands III and IV (see Fig. 6), and the overlap of bands I and II at the Γ point. The size of the two overlaps is about 0.5 eV for the p/d overlap and about 0.2 eV for the overlap at the Brillouin-zone center. These values could vary if spin-orbit interaction effects were included in the calculation.

As mentioned above, bands I and II are mainly derived from Te $5p$ orbitals at the center of the Brillouin zone. Proceeding from Γ to the Y point, the admixture of the Te $5p$ states decreases noticeably until an almost W $5d$ character prevails. The change in the orbital character from d - to p predominance indicates that the bands I and II possess a p admixture due to the hybridization with band III. These bands overlap by approximately 0.5 eV, considerably larger than the 20 meV derived from transport measurements by Kabashima.⁶ Further contradictions arise from the more complicated band structure near the Fermi level presented here. Instead of only one band we found two electronlike bands (bands I and II) overlapping with one heavy-hole band (band III).

Thus, the theoretical electronic band structure of Td-WTe₂ indicates both semimetallic and metallic band characteristics that cause the transport properties. According to the semimetallic character Td-WTe₂ reveals a direct p/d overlap. This deviates considerably from the standard semimetallic band scheme. Semimetals like TiTe₂ (Refs. 31 and 32) are characterized by an indirect p/d overlap. The tendency of WTe₂ to form a semimetallic band scheme was also proposed by Kabashima.⁶ However, we found two additional metallic bands that also classify WTe₂ as a metal. But due to their large dispersion one would directly expect low density-of-states at the Fermi level in line with the calculations (Sec. III). As a consequence, it is clear that the conductivity of WTe₂ is rather low.

The experimental data is in good agreement with the LDA results. In particular, in the Γ Z direction one Fermi-level crossing proposed by the theory is indicated in the EDC’s. Especially the discontinuous dispersion and drop of the intensity favors this interpretation. In addition, however, the theory also predicts further Fermi-level crossings which cannot be experimentally observed, in particular in the directions Γ -Z and Γ -Y. Especially along Γ -Y, the Fermi-level crossings of the LDA bands III and I (see Fig. 6) do not occur experimentally. Therefore, in the Γ Y direction the p/d overlap, cannot be observed. Consequently Td-WTe₂ with its experimentally indicated conduction bands along Γ -Z and Γ -Y could be a metal with low density-of-states at E_F . Notwithstanding, there is a weak experimental shoulder beyond those \mathbf{k} -space Fermi-level crossing positions of bands III and I (up to $\vartheta = 13^\circ$), which were predicted by the theory (see Figs. 12 and 14). If one follows the dispersion of this shoulder from $\vartheta = 13^\circ$ to $\vartheta = 9^\circ$ it can be assumed that there are further conduction bands in the direction Γ -Y, which cause a p/d overlap. Here, highly resolved measurements at low temperatures are necessary.

The effect of the distorted crystal structure on the band structure of WTe₂ still remains unclear. Additional calculations for an 1T structure indicate that the octahedral distort-

tions favor an increased p - d hybridization. As a consequence, we expect the $W 5d$ bands to shift to higher-binding energies relative to the undistorted tungsten dichalcogenides—which is indeed observable.

VIII. SUMMARY

We have studied the electronic band structure of the distorted layered compound Td-WTe₂ in both angle-resolved photoemission spectroscopy and density-functional theory in local-density approximation. The three-dimensional experimental band structure of this material has been worked out. The overriding features of the valence band structure of Td-WTe₂ discussed in Sec. VI, show that the combined results of experiment and theory are in good agreement. Also in the low-energy range the angle-resolved photoelectron spectroscopy (ARPES) data appears to confirm the existence of two conduction bands in the directions Γ - Z and Γ - Y . Furthermore, some differences between theory and experiment exist, particularly in the low-energy range near E_F . The theory reveals a band structure with a direct p/d overlap. This band scheme deviates considerably from the classical semimetallic scheme. Semimetals are typically charac-

terized by an indirect band overlap. In contrast to this, the present theoretical study reveals for Td-WTe₂ a direct overlap of about 0.5 eV. This value is considerably larger than that assumed in previous theoretical work. The purely semimetallic band scheme is altered in the case of Td-WTe₂ by the addition of two metallic LDA bands. For this reason, Td-WTe₂ could be classified as an intermediate between a semimetal and a metal with a low density-of-states at the Fermi level. The ARPES data cannot confirm the existence of a p/d overlap in the ΓY direction. However, in the ΓY direction there are experimental indications for further Fermi-level crossings as a weak photoemission structure between $\vartheta=9^\circ$ and $\vartheta=13^\circ$ shows. Close to the Fermi level, in particular, more highly resolved photoemission measurements are necessary along Γ - Y .

ACKNOWLEDGMENTS

We would like to thank D. Kaiser for her support in crystal growth. Furthermore, we would like to thank Dr. S. Rogaschewski for performing the EDX analysis. This work received funding from the BMBF under Project No. 05 622 KHA.

*Email: jan.augustin@physik.hu-berlin.de

[†]Present address: Berliner Elektronenspeicherring-Gesellschaft für Synchrotronstrahlung m. b. H., Rudower Chaussee 5, 12489 Berlin.

¹A. Goldmann, T. Ishii, R. Manzke, J. R. Naegele, and M. Skibowski, in *Electronic Structure of Solids: Photoemission Spectra and Related Data*, edited by A. Goldman (Springer, Berlin, 1994); Landolt-Börnstein, *Numerical Data and Functional Relationships in Science and Technology, New Series*, edited by O. Madelung and W. Martienssen, Group III: Solid State Physics, Vol. 23, Subvolume B.

²W. Y. Liang, NATO ASI Ser., Ser. B **148** (1986).

³J. A. Wilson and A. D. Yoffe, *Adv. Phys.* **18**, 193 (1969).

⁴W. G. Dawson and D. W. Bullett, *J. Phys. C* **20**, 6159 (1987).

⁵L. H. Brixner, *J. Inorg. Nucl. Chem.* **24**, 257 (1962).

⁶S. Kabashima, *J. Phys. Soc. Jpn.* **21**, 945 (1966).

⁷B. E. Brown, *Acta Crystallogr.* **20**, 268 (1966).

⁸S. L. Lang, R. V. Kasowski, and B. A. Parkinson, *Phys. Rev. B* **39**, 9987 (1989).

⁹S. L. Lang, R. V. Kasowski, A. Suna, and B. A. Parkinson, *Surf. Sci.* **238**, 280 (1990).

¹⁰A. Crossley, S. Myhra, and C. J. Sofield, *Surf. Sci.* **318**, 39 (1989).

¹¹H. Bengel, S. N. Magonov, D. Jung, J. Ren, M.-H. Whangbo, and H.-J. Cantow, *New J. Chem.* **20**, 287 (1996).

¹²P. Hohenberg and W. Kohn, *Phys. Rev.* **136**, B864 (1964).

¹³W. Kohn and L. J. Sham, *Phys. Rev.* **140**, A1133 (1965).

¹⁴A. R. Williams, J. Kübler, and C. D. Gelatt, Jr., *Phys. Rev. B* **19**, 6094 (1979).

¹⁵V. Eyert, Ph.D. thesis, Technische Hochschule Darmstadt, 1991.

¹⁶J. Kübler and V. Eyert, *Electronic and Magnetic Properties of Metals and Ceramics*, edited by K. H. J. Buschow (VCH Verlagsgesellschaft, Weinheim, 1992), pp. 1–145; *Materials Science and Technology*, edited by R. W. Cahn, P. Haasen, and E.

J. Kramer, Volume 3A of the series (VCH Verlagsgesellschaft, Weinheim, 1992).

¹⁷V. Eyert, special issue of *Int. J. Quantum Chem.* **77**, 1007 (2000).

¹⁸V. Eyert, in *Density Functional Methods: Applications in Chemistry and Material Science*, edited by M. Springborg (Wiley, Chichester, 1997), p. 233.

¹⁹R. Claessen, Th. Straub, P. Steiner, S. Hüfner, V. Eyert, R. O. Anderson, J. W. Allen, C. Janowitz, and C. G. Allen, *Physica B* **230-232**, 294 (1997).

²⁰Th. Straub, R. Claessen, P. Steiner, S. Hüfner, V. Eyert, K. Friemelt, and E. Bucher, *Phys. Rev. B* **55**, 13 473 (1997).

²¹O. K. Andersen, *Phys. Rev. B* **12**, 3060 (1975).

²²V. Eyert and K.-H. Höck, *Phys. Rev. B* **57**, 12 727 (1998).

²³V. Eyert, *J. Comput. Phys.* **124**, 271 (1996).

²⁴V. Eyert (calculations unpublished).

²⁵J. Augustin, Th. Böker, A. Müller, N. Orłowski, C. Janowitz, and R. Manzke, *HASYLAB Ann. Rep.* **I**, 295 (1996).

²⁶Th. Straub, K. Fauth, Th. Finteis, M. Hengsberger, R. Claessen, P. Steiner, and S. Hüfner, *Phys. Rev. B* **53**, R16 152 (1996).

²⁷J. Augustin, A. Müller, N. Orłowski, C. Janowitz, and R. Manzke (unpublished).

²⁸Th. Finteis, M. Hengsberger, Th. Straub, K. Fauth, R. Claessen, P. Auer, P. Steiner, and S. Hüfner, *Phys. Rev. B* **55**, 10 400 (1997).

²⁹M. Traving, M. Boehme, L. Kipp, F. Starrost, E. E. Krasovskii, A. Perlov, W. Schatke, and M. Skibowski, *Phys. Rev. B* **55**, 10 392 (1997).

³⁰S. Hüfner, *Photoelectron Spectroscopy* (Springer, Berlin, 1995).

³¹R. Claessen, R. O. Anderson, J. W. Allen, C. G. Olson, C. Janowitz, W. P. Ellis, S. Harm, M. Kalning, R. Manzke, and M. Skibowski, *Phys. Rev. Lett.* **69**, 808 (1992).

³²R. Claessen, R. O. Anderson, G.-H. Gweon, J. W. Allen, W. P. Ellis, C. Janowitz, C. G. Olson, Z. X. Shen, V. Eyert, M. Skibowski, K. Friemelt, E. Bucher, and S. Hüfner, *Phys. Rev. B* **54**, 2453 (1996).